J Appl Physiol 103: 1366–1378, 2007.
First published 28 June, 2007; doi:10.1152/japplphysiol.00489.2007.

Model of oxygen transport and metabolism predicts effect of hyperoxia on canine muscle oxygen uptake dynamics

Nicola Lai,[1,3] Gerald M. Saidel,[1,3] Bruno Grassi,[5] L. Bruce Gladden,[6] and Marco E. Cabrera[1,2,3,4]

Departments of [1]Biomedical Engineering and [2]Pediatrics and [3]Center for Modeling Integrated Metabolic Systems, Case Western Reserve University and [4]Rainbow Babies and Children's Hospital, Cleveland, Ohio; [5]Dipartimento di Scienze e Tecnologie Biomediche, Universita' degli Studi di Milano, Italy; and [6]Department of Kinesiology, Auburn University, Alabama

Submitted 4 May 2007; accepted in final form 27 June 2007

Lai N, Saidel GM, Grassi B, Gladden LB, Cabrera ME. Model of oxygen transport and metabolism predicts effect of hyperoxia on canine muscle oxygen uptake dynamics. *J Appl Physiol* 103: 1366–1378, 2007. First published 28 June, 2007; doi:10.1152/japplphysiol.00489.2007.— Previous studies have shown that increased oxygen delivery, via increased convection or arterial oxygen content, does not speed the dynamics of oxygen uptake, $\dot{V}O_{2m}$, in dog muscle electrically stimulated at a submaximal metabolic rate. However, the dynamics of transport and metabolic processes that occur within working muscle in situ is typically unavailable in this experimental setting. To investigate factors affecting $\dot{V}O_{2m}$ dynamics at contraction onset, we combined dynamic experimental data across working muscle with a mechanistic model of oxygen transport and metabolism in muscle. The model is based on dynamic mass balances for O_2, ATP, and PCr. Model equations account for changes in cellular ATPase, oxidative phosphorylation, and creatine kinase fluxes in skeletal muscle during exercise, and cellular respiration depends on [ADP] and [O_2]. Model simulations were conducted at different levels of arterial oxygen content and blood flow to quantify the effects of convection and diffusion of oxygen on the regulation of cellular respiration during step transitions from rest to isometric contraction in dog gastrocnemius muscle. Simulations of arteriovenous O_2 differences and $\dot{V}O_{2m}$ dynamics were successfully compared with experimental data (Grassi B, Gladden LB, Samaja M, Stary CM, Hogan MC. *J Appl Physiol* 85: 1394–1403, 1998; and Grassi B, Gladden LB, Stary CM, Wagner PD, Hogan MC. *J Appl Physiol* 85: 1404–1412, 1998), thus demonstrating the validity of the model, as well as its predictive capability. The main findings of this study are: *1*) the estimated dynamic response of oxygen utilization at contraction onset in muscle is faster than that of oxygen uptake; and *2*) hyperoxia does not accelerate the dynamics of diffusion and consequently muscle oxygen uptake at contraction onset due to the hyperoxia-induced increase in oxygen stores. These in silico derived results cannot be obtained from experimental observations alone.

THE OXYGEN CONSUMPTION RESPONSE to a step-like increase in energy demand has been studied extensively over the last few decades at various biological scales and under a variety of conditions (4, 26, 27, 35, 40, 41, 53, 64). Indeed, oxygen consumption dynamics in response to various stimuli have been investigated in isolated mitochondria (10, 11), isolated myocytes (62), muscle microvasculature (49), and isolated muscle preparations in situ (24), as well as in whole organisms (21, 68). Collectively, these experimental approaches have provided valuable information and insights into the role of potential factors and mechanisms controlling cellular respiration. Each of these experimental approaches has its own intrinsic strengths and limitations, and data obtained through these methods have both confirmed conclusions inferred at a different biological level and exposed inconsistencies. Specifically, while pulmonary oxygen uptake dynamics, $\dot{V}O_{2p}$, agrees within 10% with those of muscle oxygen uptake, $\dot{V}O_{2m}$ (21), measurements conducted in isolated mitochondria (57) indicate that O_2 consumption and ATP synthesis derived from oxidative metabolism respond very rapidly to a step increase in energy demand (τ = 500 ms). The experimental evidence is that the characteristic dynamics of muscle $\dot{V}O_{2m}$ in vivo are two orders of magnitude slower than those of mitochondrial O_2 consumption in vitro. This discrepancy highlights the urgent need for further studies of possible rate-limiting steps or processes that buffer the signals that turn on oxidative phosphorylation at the cellular level. Despite the fact that the basic pathways of cellular energy metabolism were deciphered and characterized in vitro over 50 years ago, today there is no consensus on how these pathways interact and are controlled in vivo. Specifically, the complex controls and coordination of ATP synthesis derived from oxidative metabolism are yet to be elucidated during the transition from one rate of ATP utilization to another (30).

The fundamental question in the study of "$\dot{V}O_2$ kinetics" at the onset of exercise is, which are the factors that control the dynamics of $\dot{V}O_2$ at the cellular, muscular, and organism level? At exercise onset, skeletal muscle must sustain very large-scale changes in ATP turnover rate (30, 31) while maintaining a constant [ATP]. This requires coordinated variations in the ATP synthesis pathways to closely match ATP utilization. However, ATP utilization increases almost instantaneously at exercise onset, while the time course of the rate of aerobically derived ATP synthesis lags behind that of ATP hydrolysis and rises monotonically in an exponential pattern towards its steady state. Both the dynamics of O_2 transport to mitochondria and its utilization in the electron transport chain may play critical roles in ATP homeostasis during this transition. Moreover, the dynamics of these processes depend on the interaction of multiple physical, physiological, and/or biochemical factors (35, 59).

Oxygen transport from blood to muscle mitochondria during increased energy demand depends on the dynamics of muscle blood flow (Q) and the oxygen rate of diffusion ($J_{O_{2m}}$) from

Address for reprint requests and other correspondence: Marco E. Cabrera, Pediatric Cardiology, MS-6011, Case Western Reserve Univ., 11100 Euclid Ave., RBC 389, Cleveland, OH 44106-6011 (e-mail: mec6@cwru.edu).

The costs of publication of this article were defrayed in part by the payment of page charges. The article must therefore be hereby marked "*advertisement*" in accordance with 18 U.S.C. Section 1734 solely to indicate this fact.

tissue capillaries to cells. In vivo, however, oxygen utilization depends not only on the concentration of the products of ATP hydrolysis, but also on the concentrations and activities of the respiratory chain enzymes, mitochondrial [O_2], and supply of reducing equivalents. To date it is still controversial whether the dynamics of skeletal muscle O_2 consumption at the onset of exercise is limited by intrinsic metabolic properties or by the transport of O_2 to the mitochondria (i.e., O_2 delivery limitation) (59).

In studies utilizing the isolated canine gastrocnemius muscle preparation (32), greater changes in the putative controllers of cellular respiration (PCr and ATP) were required to achieve a given power output when arterial oxygen content was decreased. These results indicate that the intracellular concentration of oxygen plays a major role in modulating cellular respiration. In general, the oxygenation state of the contracting muscle depends on the supply of oxygen (blood flow, arterial oxygen content) as well as the oxygen demand determined by the metabolic rate. Follow up studies demonstrated that at a metabolic rate equivalent to 60% of $\dot{V}O_{2m,peak}$, neither enhanced blood oxygen content nor enhanced convective/diffusive oxygen delivery accelerated the dynamics of muscle oxygen uptake (22, 23). In contrast, when the imposed oxygen demand was near $\dot{V}O_{2m,peak}$, enhanced convective oxygen delivery enabled a faster $\dot{V}O_{2m}$ dynamic response than when the delivery of oxygen was spontaneous (24). Based on these findings, it was concluded that both oxygen delivery and the oxidative metabolic machinery determine $\dot{V}O_{2m}$ dynamics at the onset of contraction and that these factors affect $\dot{V}O_{2m}$ dynamics differently depending on the exercise intensity.

These conclusions, however, were derived from muscle oxygen uptake dynamics, $\dot{V}O_{2m}$, obtained from measurements of blood flow and arteriovenous O_2 concentration differences across a contracting muscle and not from direct measurements of muscle O_2 utilization dynamics, UO_{2m}. Moreover, the dynamic responses of oxygen concentration in tissue or other key muscle metabolites were partially obtained during the transition from rest to sustained contraction. In light of the inherent limitations of the experimental measurements in vivo, a mathematical model that describes the complex interactions among factors affecting oxygen utilization and delivery is needed to investigate the factors regulating respiration during exercise. A theoretical-experimental approach for investigating O_2 transport and metabolism in skeletal muscle can quantify the extent to which convective/diffusive processes and critical levels of mitochondrial po_2 affect the regulation of respiration in vivo, at exercise onset. To our knowledge, no computational model of oxygen transport and bioenergetics in contracting skeletal muscle has been validated and used to predict the dynamics of oxygen transport to and metabolic processes in tissue cells in vivo, dynamics which are difficult if not impossible to obtain experimentally.

This study extends a bioenergetics model (42, 60) that is integrated with a spatially distributed model of oxygen transport and exchange between blood and tissue. Optimal estimate of the model parameter was obtained by least-squares fitting with experimental data acquired during electrical stimulation of the dog gastrocnemius muscle in situ (23). With that parameter value, model simulations were used to predict the dynamic responses of arteriovenous O_2 concentration difference, C^{T}_{A-V}, and $\dot{V}O_{2m}$ to a step change in metabolic rate under experimental conditions (22, 23). Dynamic changes in metabolic fluxes and concentrations in tissue cells were predicted to elucidate the role of several factors influencing oxygen exchange in blood and tissue within the muscle during a step change in metabolic rate. Specifically, model simulations of [O_2] dynamics in blood and tissue, tissue [ATP] and [PCr], as well as the dynamic responses of the rates of ATPase, oxidative phosphorylation, and creatine kinase obtained under corresponding experimental conditions were used to test the following hypotheses:

First, the dynamics of $\dot{V}O_{2m}$ is slower than the corresponding muscle oxygen consumption UO_{2m}, regardless of the arterial oxygen content.

Second, the dynamics of UO_{2m} at the onset of moderate intensity exercise remain the same regardless of the arterial oxygen content and the dynamics of oxygen delivery. In contrast, the dynamics of $\dot{V}O_{2m}$ and JO_{2m} during hyperoxia lag behind the corresponding $\dot{V}O_{2m}$ and JO_{2m} obtained during normoxia.

METHODS

Glossary

C_A	Total concentration of ADP and ATP (mM)
C_{ADP}	Concentration of ADP in tissue (mM)
C_{ATP}	Concentration of ATP in tissue (mM)
C_C	Total concentration of PCr and Cr (mM)
C_{Cr}	Concentration of Cr in tissue (mM)
C_{PCr}	Concentration of PCr in tissue (mM)
C_{Hb}	Concentration of Hb in blood (mM)
$C_{rbc,Hb}$	Concentration of Hb in the red blood cell (mM)
$C_{mc,Mb}$	Concentration of Mb in myocyte (mM)
$C^{B}_{O_2,x}$	Bound oxygen concentration in artery, capillary, and tissue (mM)
$C^{F}_{O_2,x}$	Free oxygen concentration in artery, capillary, and tissue (mM)
$C^{T}_{O_2,x}$	Total oxygen concentration in artery, capillary, and tissue (mM)
D_b	Effective dispersion coefficient in blood (l^2/min)
D_c	Effective dispersion coefficient in tissue (l^2/min)
f_b	Blood capillary volume fraction in muscle
f_c	Extra-vascular muscle tissue volume fraction in muscle
Hct	Hematocrit (fraction of red blood cells in blood)
k_{ATPase}	ATPase rate constant (min^{-1})
K_{eq}	Equilibrium constant in CK flux
K_{Hb}	Hill constant at which Hb is 50% saturated by O_2 (mM^{-n})
K_{Mb}	Hill constant at which Mb is 50% saturated by O_2 (mM^{-1})
K_{ADP}	Michaelis Menten constant in CK flux (mM)
K_b	Michaelis Menten constant in CK flux (mM)
K_{ia}	Dissociation constant in CK flux (mM)
K_{ib}	Dissociation constant in CK flux (mM)
K_{iq}	Dissociation constant in CK flux (mM)
K_m	Michaelis Menten constant in Oxidative Phosph. flux (mM)
K_p	Michaelis Menten constant in CK flux (mM)
jO_{2m}, JO_{2m}	Capillary-tissue transport rate of oxygen (mM/min)
n	Hill coefficient
PO_2	Oxygen partial pressure (mmHg)
PS	Permeability surface area product ($l \cdot l^{-1} \cdot min^{-1}$)

PS^{max}	Maximal value of Permeability surface area product ($l \cdot l^{-1} \cdot min^{-1}$)
PS^{rest}	Permeability surface area product at rest ($l \cdot l^{--1} \cdot min^{-1}$)
Q, Q_m	Muscle blood flow (l/min, $1 \cdot l^{-1} \cdot min^{-1}$)
t	Time (min)
t_0	Time at the onset of contraction (min)
uO_{2m}, U_{O2m}	Muscle oxygen utilization (mM/min)
V^f_{CK}	Maximal forward flux of CK reaction (mM/min)
V_{max}	Maximal flux of oxidative Phosphorylation (mM/min)
V_{cap}, V_{mus}, V_{tis}	Anatomical volume of capillary, muscle, and tissue, respectively (l)
$\dot{V}_{O2m}$	Muscle oxygen uptake (mM/min)
$\dot{V}_{O2m,peak}$	Maximal muscle oxygen uptake (mM/min)
W_{mc}	Myocyte volume fraction
$\langle y(t) \rangle$	Spatial average variable (mmHg, nM, mM/min)

Greek Letters

α_{O_2}	Oxygen solubility in blood (mM/mmHg)
β	P/O_2 ratio
$\Delta\phi_{CK}$	Net metabolic flux of creatine kinase (mM/min)
ϕ_{ATPase}	ATPase metabolic flux (mM/min)
ϕ^f_{CK}	CKase forward metabolic flux (mM/min)
ϕ^r_{CK}	CKase reverse metabolic flux (mM/min)
ϕ_{OxPhos}	Oxidative phosphorylation metabolic flux (mM/min)
γ_b	Derivative term
γ_c	Derivative term
υ	Volume coordinate (l)
τ_{PCr}	Time constant of the PCr kinetics (s)
τ_Q	Time constant of the muscle blood flow (s)
$\tau_{UO_{2m}}$	Time constant of the muscle oxygen utilization (s)

Superscripts

B	Bound oxygen concentration
exp	Experimental data
F	Free oxygen concentration
mod	Model simulation
R	Resting condition
S	Stimulus condition
SS	Steady state
T	Total oxygen concentration

Subscripts

art	Artery
b	Blood
c	Cell
cap	Capillary
mus	Muscle
tis	Tissue
ven	Venous
A–V	Arteriovenous difference

Dynamic mass balances. The metabolic response of skeletal muscle to a stimulus can be described by transport and metabolic processes associated with oxygen, ATP, and PCr (Fig. 1). We consider the total muscle volume to consist primarily of capillary blood and extravascular muscle tissue, $V_{mus} = V_{cap} + V_{tis}$. Oxygen concentration dynamics in skeletal muscle are represented by spatially distributed mass balances (derived in Appendix). Free oxygen concentrations in the capillary blood, $C^F_{O2,b}(v,t)$, and in muscle cells, $C^F_{O2,c}(v,t)$, depend on time (t) and tissue location as indicated by the cumulative muscle volume (v) from the arterial input v = 0 to the venous output v = V_{mus}. (Variables and symbols are defined in the Glossary.)

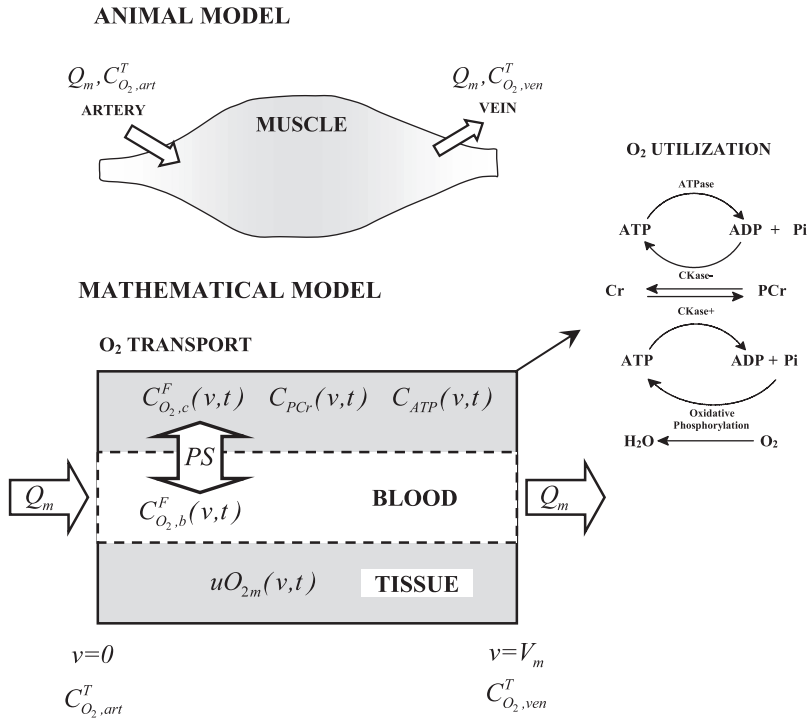

Fig. 1. Schematic representation of oxygen transport and consumption within the gastrocnemius muscle showing the link between muscle oxygen uptake, $\dot{V}_{O2m}(t)$, and the heterogeneity of muscle oxygen consumption, $U_{O2m}(t)$.

O_2 UPTAKE $$VO_{2m}(t) = Q_m(t)\left(C^T_{O_2,art} - C^T_{O_2,ven}(t)\right)$$

O_2 UTILIZATION $$UO_{2m}(t) = \langle uO_{2m}(t) \rangle$$

The dynamic, spatial distribution of free oxygen concentration in capillary blood is

$$f_b \frac{\partial C^F_{O_2,b}}{\partial t} = -Q \frac{\partial C^F_{O_2,b}}{\partial v} + D_b \frac{\partial^2 C^F_{O_2,b}}{\partial v^2} - \frac{PS}{\gamma_b}(C^F_{O_2,b} - C^F_{O_2,c}) \qquad 0 < v < V_{mus} \tag{1}$$

The first term on the right side represents convective transport in the direction of flow Q in which $f_b = V_{cap}/V_{mus}$ is the ratio of capillary blood volume to total muscle volume; the second term represents axial dispersion characterized by an effective dispersion coefficient D_b (1); the third term represents transport between capillary blood and extravascular muscle cells. Capillary-tissue transport depends on the permeability-surface area, PS, and the change of total oxygen concentration with respect to free oxygen concentration, γ_b, (see Appendix). During exercise, the permeability-surface area is assumed to change with the same dynamic pattern as the muscle blood flow Q (8). Corresponding to a step-up change of Q with characteristic time constant τ_Q, the capillary-tissue transport rate between resting and maximal steady states is represented by:

$$PS(t) = PS^{rest} + (PS^{max} - PS^{rest})[1 - \exp(t_0 - t)/\tau_Q] \qquad t > t_0 \tag{2}$$

where PS^{max} is the maximal value and PS^{rest} is the value at resting, steady state when $t \leq t_0$.

The dynamic, spatial distribution of free oxygen concentration $C^F_{O_2,c}(v,t)$ in muscle cells of extravascular tissue is

$$f_c \frac{\partial C^F_{O_2,c}}{\partial t} = D_c \frac{\partial^2 C^F_{O_2,c}}{\partial v^2} + \frac{PS}{\gamma_c}(C^F_{O_2,b} - C^F_{O_2,c}) - \frac{uO_{2m}}{\gamma_c} \qquad 0 < v < V_{mus} \tag{3}$$

where D_c is an effective dispersion coefficient in muscle tissue; $f_c = V_{tis}/V_{mus}$ is the ratio of extravascular muscle tissue volume to total muscle volume; γ_c is the change of total oxygen concentration with respect to free oxygen concentration in muscle cells. The oxygen utilization rate per unit volume of total muscle volume is proportional to the oxidative phosphorylation flux, $uO_{2m} = f_c \phi_{OxPhos}$.

The metabolic reaction processes that involve oxidative phosphorylation are associated with the concentration dynamics of ATP and PCr (Fig. 1). Because of their dependence on $C^F_{O_2,c}(v,t)$, the concentrations $C_{ATP}(v,t)$ and $C_{PCr}(v,t)$ are implicitly spatially distributed in muscle. In dynamic mass balances, these concentrations are related to metabolic fluxes:

$$\frac{\partial C_{ATP}}{\partial t} = -\phi_{ATPase} + \beta\phi_{OxPhos} + \Delta\phi_{CK} \tag{4}$$

$$\frac{\partial C_{PCr}}{\partial t} = -\Delta\phi_{CK} \tag{5}$$

where ϕ_{ATPase} is the ATP utilization flux, β is the stoichiometric coefficient that relates oxidative phosphorylation to ATP production, and $\Delta\phi_{CK}$ is the net forward flux of the creatine kinase reaction. The metabolic fluxes are functions of O_2, ADP, ATP, PCr, and Cr. However, the concentration pairs ATP-ADP and PCr-Cr are related by mass conservation of adenosine and creatine, respectively, whose total concentrations C_A and C_C are constant:

$$C_A = C_{ADP} + C_{ATP}; \qquad C_C = C_{Cr} + C_{PCr} \tag{6a,b}$$

Metabolic fluxes. The flux relationships for this model have been presented previously (42). The oxidative phosphorylation flux is nonlinearly related to the ADP and oxygen:

$$\phi_{OxPhos} = V_{max}\left(\frac{C_{ADP}}{K_{ADP} + C_{ADP}}\right)\left(\frac{C^F_{O_2,c}}{K_m + C^F_{O_2,c}}\right) \tag{7}$$

The flux of the ATPase reaction is proportional to the ATP concentration:

$$\phi_{ATPase} = k_{ATPase} C_{ATP} \tag{8}$$

where k_{ATPase} changes with a metabolic stimulus. The net forward and reverse reaction fluxes of creatine kinase are nonlinearly related to concentrations of energy phosphates:

$$\Delta\phi_{CK} = \phi^f_{CK} - \phi^r_{CK} = \frac{\frac{V^f_{CK}}{K_b K_{ia}}\left(C_{ADP}C_{PCr} - \frac{C_{Cr}C_{ATP}}{K_{eq}}\right)}{1 + \frac{C_{ADP}}{K_{ia}} + \frac{C_{ATP}}{K_{iq}} + \frac{C_{PCr}}{K_{ib}} + \frac{C_{ADP}C_{PCr}}{K_b K_{ia}} + \frac{C_{Cr}C_{ATP}}{K_{iq}K_p}} \tag{9}$$

Boundary and initial conditions. The boundary conditions for the capillary blood assume that the input oxygen concentration from arterial blood is known and that the output oxygen concentration leaving the capillaries has a negligible gradient:

$$v = 0 \quad C^F_{O_2,b} = C^F_{O_2,art}; \qquad v = V_{mus} \quad \frac{\partial C^F_{O_2,b}}{\partial v} = 0; \tag{10}$$

The oxygen gradients are negligible at the arterial and venous sides of the tissues (15):

$$v = 0 \quad \frac{\partial C^F_{O_2,C}}{\partial v} = 0; \qquad v = V_{mus} \quad \frac{\partial C^F_{O_2,c}}{\partial v} = 0; \tag{11}$$

Initially, the concentrations are distributed in a resting, steady state:

$$t = t_0 \quad C^F_{O_2,b} = C^{F,rest}_{O_2,b}(v); \quad C^F_{O_2,c} = C^{F,rest}_{O_2,c}(v); \quad C^F_{ATP} = C^{F,rest}_{ATP}(v); \quad C^F_{PCr} = C^{F,rest}_{PCr}(v) \tag{12}$$

Model simulation and parameter estimation. The primary data available for comparison to model simulation consist of the arteriovenous concentration difference of oxygen, $C^T_{A-V}(t) = C^T_{O_2,art} - C^T_{O_2,ven}$, and the rate of muscle oxygen uptake

$$VO_{2m}(t) = Q(t)[C^T_{O_2,art} - C^T_{O_2,ven}(t)]/V_{mus} \tag{13}$$

(total oxygen concentration is related to free oxygen concentration by the oxygen equilibrium relationship $C^T_{O_2} = g[C^F_{O_2}]$ as presented in the Appendix). The C^T_{A-V} and $\dot{V}O_{2m}$ data (Table 1), are responses from gastrocnemius muscle in situ to tetanic stimuli at several levels of arterial oxygen content (22, 23). Stimulation by isometric contraction corresponded to 60–70% of peak $\dot{V}O_{2m}$. In three experiments, the blood flow is externally controlled at a constant level, while in the fourth blood flow is spontaneous according to the electrical stimulus. The different experimental conditions were simulated by using corresponding values of model parameters: $kATP_{ase}$, $C^F_{O2,art}$, and Q_m.

At steady state, rate of muscle oxygen uptake equals the rate of muscle oxygen utilization per unit muscle volume:

Table 1. *Experimental conditions in studies of skeletal muscle simulation*

Experiment	O_2 Content, $Po_{2,art}$ (mmHg)	Perfusion, Q (mL·100g^{-1}·min^{-1})	Reference
Hyperoxia + RSR-13, PP	494	89	23
Hyperoxia, PP	509	89	23
Normoxia, PP	79	93	22
Normoxia, SP	86	Q(t)	22

PP, pump-perfused; SP, self-perfused.

$$VO_{2m}^{ss} = UO_{2m}^{ss} \quad (14)$$

At any time the total (average) oxygen utilization in muscle is

$$UO_{2m}(t) = \int_0^{V_{mus}} uO_{2m}(v,t)dv/V_{mus} = \langle uO_{2m}(t)\rangle \quad (15)$$

A general expression for any spatial average variable in this model depends on a specific volume:

$$\langle y(t)\rangle = \int_0^{V_x} y(v,t)dv/V_x \quad V_x = V_{cap}, V_{tis}, V_{mus} \quad (16)$$

Of special interest is the volume-averaged capillary-tissue transport rate of oxygen between blood and muscle cells:

$$JO_{2m}(t) = PS \int_0^{V_{mus}} (C_{O_2,b}^F(v,t) - C_{O_2,c}^F(v,t))dv/V_{mus} = \langle jO_{2m}(t)\rangle \quad (17)$$

Values of most parameters in this model are available from previous studies (Tables 2 and 3). The parameter values in Table 2 apply to all experiments and are independent of the input conditions. The effective dispersion parameters are arbitrarily chosen to be sufficiently small because the effects of dispersion processes are small compared with other transport and metabolic processes. The parameter values in Table 3 depend on experimental conditions. The unknown model parameters, reaction rate coefficients of the ATPase flux, k_{ATPase}, and of the oxidative phosphorylation flux, V_{max}, must be estimated.

At steady state, when $\Delta\phi_{CK}$ is negligible, the value of k_{ATPase} can be determined from the steady state of Eq. (3):

$$C_{ATP}^{ss}k_{ATPase} = \beta\phi_{OXphos}^{ss} = \beta uO_{2m}^{ss}/f_c \quad (18)$$

Upon integration over muscle volume, this leads to

$$\langle C_{ATP}^{ss}\rangle k_{ATPase} = \beta\langle uO_{2m}^{ss}\rangle f_c = \beta UO_{2m}^{ss}/f_c = \beta VO_{2m}^{ss}/f_c \quad (19)$$

Assuming that $\langle C_{ATP}^{ss}\rangle = C_{ATP}^{ss}$,

$$k_{ATPase} = \beta VO_{2m}^{ss}/(f_c C_{ATP}^{ss}) \quad (20)$$

The reaction rate coefficient V_{max} is estimated by least-squares fitting of the model simulated arteriovenous concentration difference of oxygen, $C_{A-V}^T = C_{O_2,art}^T - C_{O_2,ven}^T$, to that from experimental data. The optimal value of V_{max} is that which minimizes the least-square objective function:

$$\Gamma = \sum_{i=1}^{k}[C_{A-V}^{T,exp}(t_i) - C_{A-V}^{T,mod}(t_i;V_{max})]^2 \quad (21)$$

The minimization is accomplished by numerical optimization using an adaptive, nonlinear algorithm (DN2FB, http://www.netlib.org; 17). The data come from the experiment with the greatest free oxygen availability and constant, controlled blood flow (hyperoxia + RSR-13). Experimentally, the rate of oxygen transport was enhanced by perfusing contracting muscle with an elevated blood flow. By having the dogs breathe a hyperoxic gas mixture and by administering an allosteric inhibitor of oxygen binding to hemoglobin (hyperoxia + RSR-13), a significant right-shift of the Hb-O_2 dissociation curve was induced. The optimal estimate of V_{max} from this data is applicable to simulations of all experimental conditions in Table 1.

After parameter estimation, the mathematical model was used to predict C_{A-V}^T dynamic responses to different arterial oxygen contents and blood flow dynamics. Other outputs simulated with the model include the dynamic responses of O_2, ATP, and PCr concentrations, as well as ATPase (ϕ_{ATPase}), oxidative phosphorylation (ϕ_{OxPhos}), and net creatine kinase ($\Delta\phi_{CK}$) flux rates. The initial model concentrations depend on the experimental conditions. These are obtained by numerical solution of the dynamic mass balance equations using parameter values of Table 2. Starting with typical initial values, the model equations are solved until they converge to a resting steady state. These values become the initial conditions at which the stimulus is applied. Numerical solution of the partial differential equations is based on the method of lines (55). Through a well-developed code (DSS/2 http://www.lehigh.edu/~wes1/wes1.html), the spatial derivatives are discretized with efficient algorithms (DSS020, DSS044) of fourth-order accuracy that incorporate the boundary conditions. Consequently, the model consists of a set of ordinary differential-difference equations that constitute an initial value problem. These ordinary differential equations were solved numerically using a robust algorithm for stiff systems (DLSODE, 28).

Table 2. *Values of parameters used to simulate all experimental conditions listed in Table 1*

Notation	Value	Unit	Reference
	Values of parameters in transport equations		
α_{O_2}	$1.34\cdot10^{-3}$	mM/mmHg	33
$C_{rbc,Hb}$	5	mM	56
$C_{mc,Hb}$	0.4	mM	44
n	2.8-1.4*	NA	52
K_{Hb}	7,210.9-60†	mM^{-n}	23
K_{mb}	308.6	mM^{-1}	42
W_{mc}	0.75	NA	42
f_b	0.07	NA	42
f_c	0.93	NA	42
PS^{rest}	4	$l\cdot l^{-1}\cdot min^{-1}$	42
PS^{max}	200	$l\cdot l^{-1}\cdot min^{-1}$	42
τ_Q	17	s	22
D_b	$2.0\cdot10^{-5}$	l^2/min	Assumed
D_c	$1.2\cdot10^{-7}$	l^2/min	Assumed
	Values of parameters in metabolic equations		
C_C	20	mM	25
C_{ATP}^{SS}	6.5	mM	25
V_{CK}^f	6,000	mM/min	60
K_{eq}	177	NA	60
K_b	1.11	mM	60
K_p	3.8	mM	60
K_{ia}	0.135	mM	60
K_{ib}	3.9	mM	60
K_{iq}	3.5	mM	60
K_{ADP}	$5.8\cdot10^{-2}$	mM	60
K_m	$7\cdot10^{-4}$	mM	42

NA, not applicable. *Hill coefficient of the dissociation oxygen curve for all experimental conditions except for hyperoxia + RSR-13, where n = 1.4. †Hill constants at which Hb is 50% saturated by O_2 corresponding to P_{50} = 31.3 mmHg for all experimental conditions except for hyperoxia + RSR-13, where P_{50} = 40.1 mmHg.

RESULTS

Parameter estimation and model validation. By fitting simulated arteriovenous oxygen differences to experimental data (Fig. 2) obtained during conditions of increased oxygen delivery (hyperoxia − PP − RSR-13), optimal estimate was obtained for the maximal flux rate of oxidative phosphorylation V_{max} (14.8 mM/min). The C_{A-V}^T step response to a change in exercise intensity relative to resting is presented in Fig. 2*A*. Simulated model responses to exercise of muscle oxygen utilization, $U_{O_{2m}}$, capillary-tissue oxygen transport rate, $J_{O_{2m}}$, and muscle oxygen uptake, $\dot{V}_{O_{2m}}$, were compared with measured $\dot{V}_{O_{2m}}$ (Fig. 2*B*). The time profiles of the simulated $\dot{V}_{O_{2m}}$ correspond to experimental observations, while the simulated

Table 3. *Values of model parameters that depend on experimental conditions*

Notation	Unit	Hyperoxia + RSR-13, PP	Hyperoxia, PP	Normoxia, PP	Normoxia, SP
C_{Hb}	g/l	144	150	141	138
Hct	NA	0.446	0.465	0.437	0.428
V_{mus}	l	$63\cdot10^{-3}$	$63\cdot10^{-3}$	$92\cdot10^{-3}$	$92\cdot10^{-3}$
$P^{R}_{O_2,art}$	mmHg	494	509	79	86
$P^{R}_{O_2,ven}$	mmHg	316	285	59	57
$\dot{V}O^{R}_{2m}$	mM/min	0.31	0.36	0.40	0.24
$\dot{V}^{S}_{O_{2m}}$	mM/min	5.26	5.4	4.89	5.21
k^{R}_{ATPase}	min^{-1}	0.33	0.38	0.43	0.26
k^{S}_{ATPase}	min^{-1}	5.66	5.8	5.26	5.6

NA, not applicable. See Refs. 22 and 23.

UO_{2m} dynamic response was faster than those of JO_{2m} and $\dot{V}O_{2m}$.

The capability of the proposed mathematical model in reproducing the experimental data was further tested by considering the arteriovenous oxygen difference response to specific combinations of oxygen content and blood flow according to different in situ experiments (22, 23). In the simulations, previously estimated values of V_{max} and other common parameters were kept constant (Table 2). Other parameters dependent on the specific experimental conditions were assigned corresponding values (Table 3). The model predicted fairly well the dynamics of arteriovenous oxygen differences obtained experimentally during normoxia, with spontaneous (SP) and pumped (PP) perfusion (Fig. 3). Specifically, simulations during con-

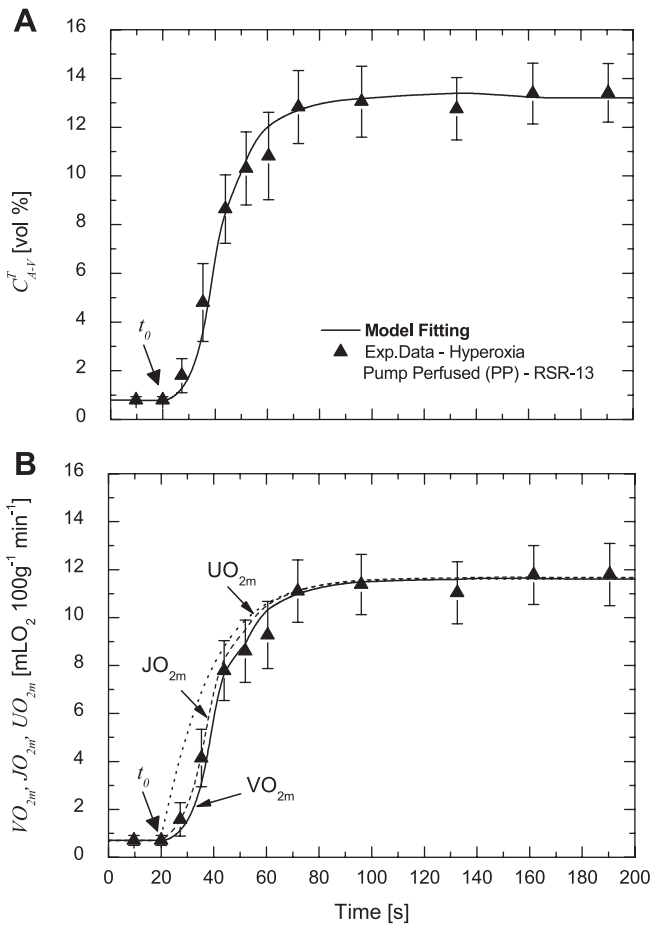

Fig. 2. Comparison between model simulation (solid lines) and experimental data (▲) for arteriovenous oxygen content differences (C^{T}_{A-V}, *A*) and muscle oxygen uptake ($\dot{V}O_{2m}$, *B*) in gastrocnemius muscle (average value of 7 dogs, ± SE) in response to step change from rest to tetanic stimulus of 60% of the $\dot{V}O_{2m,peak}$, obtained by hyperoxia + RSR-13 (see Ref. 23). Model predicted muscle oxygen utilization (UO_{2m}, dotted line) and averaged capillary-tissue transport rate of oxygen between blood and muscle cells (JO_{2m}, dashed line) under same conditions.

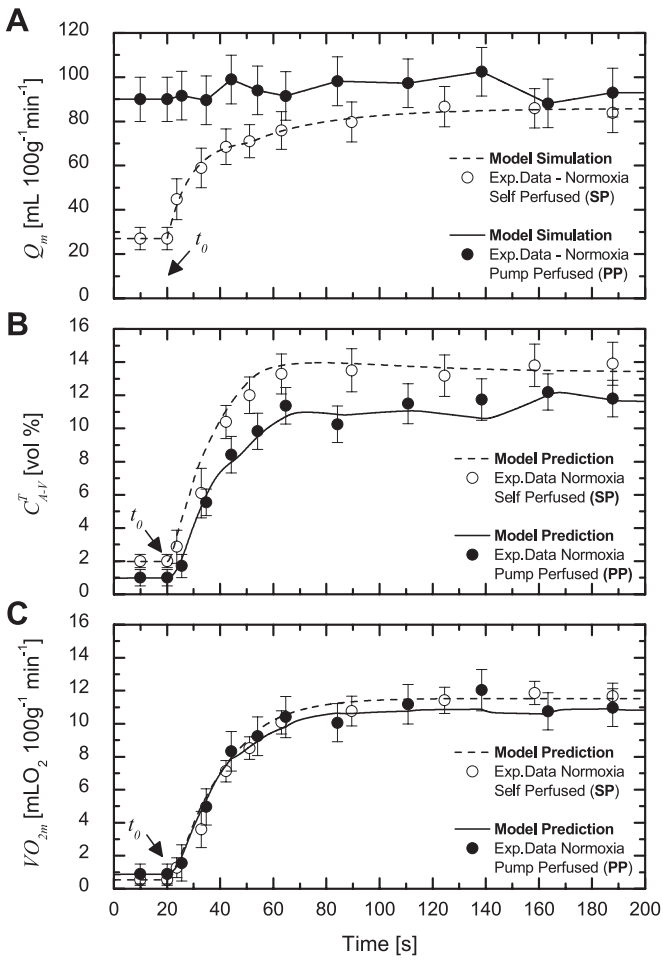

Fig. 3. Effect of the blood flow dynamics on the C^{T}_{A-V} and $\dot{V}O_{2m}$ responses across gastrocnemius muscle (average value of 5 dogs, ± SE) to step change from rest to tetanic stimulus (60% $\dot{V}O_{2m,peak}$) obtained at normoxia by pump (PP) and self perfusion (SP) (see Ref. 22). *A*: Experimental data compared with its analytical simulation used as input (Eq. 1) for model simulation of muscle blood flow (Q_m). Comparison between model prediction and experimental data of muscle arteriovenous oxygen differences, C^{T}_{A-V} (*B*), and muscle oxygen uptake, $\dot{V}O_{2m}$ (*C*) as a function of contraction time.

tractions equivalent to ~60% of peak $\dot{V}O_{2m}$ indicated that the effect of an elevated muscle blood flow profile on $\dot{V}O_{2m}$ dynamics was negligible (Fig. 3*C*). Thus, $\dot{V}O_{2m}$ dynamics obtained with both perfusion profiles were indistinguishable, even though C^{T}_{A-V} dynamics (Fig. 3*B*) were different under spontaneous and controlled perfusion (Fig. 3*A*).

Effect of hyperoxia on oxygen transport. To investigate the effect of hyperoxia on oxygen transport to tissue and the dynamics of muscle oxygen concentration and utilization, we compared model behavior during a rest-work transition (~60–70% peak $\dot{V}O_{2m}$) at an elevated blood flow (PP), under normoxia and hyperoxia (Fig. 4). Model simulations of the dynamic responses of C^{T}_{A-V} (Fig. 4*A*) and $\dot{V}O_{2m}$ (Fig. 4*B*) under normoxic and hyperoxic conditions, respectively, described fairly well the corresponding experimental data. In addition, simulations provide a comparison of dynamic responses of volume-average capillary-tissue transport rate of oxygen, JO_{2m}, muscle oxygen uptake, $\dot{V}O_{2m}$, and utilization, UO_{2m}. These are normalized to their steady-state values, JO^{ss}_{2m}, $\dot{V}O_{2m}$ and UO_{2m} respectively, under normoxia (Fig. 5*A*) and hyperoxia (Fig. 5*B*). While the UO_{2m} dynamic response was the same regardless of arterial oxygen content, the JO_{2m} dynamic response was similar to that of UO_{2m} only during normoxia (Fig. 5*A*). During hyperoxia (Fig. 5*B*), however, JO_{2m} displayed a sluggish behavior in the first 10 s after contraction onset. In both cases, the UO_{2m} dynamic response was faster than that of JO_{2m} and $\dot{V}O_{2m}$ (Fig. 5), as quantified by the mean response times (Table 4) (42).

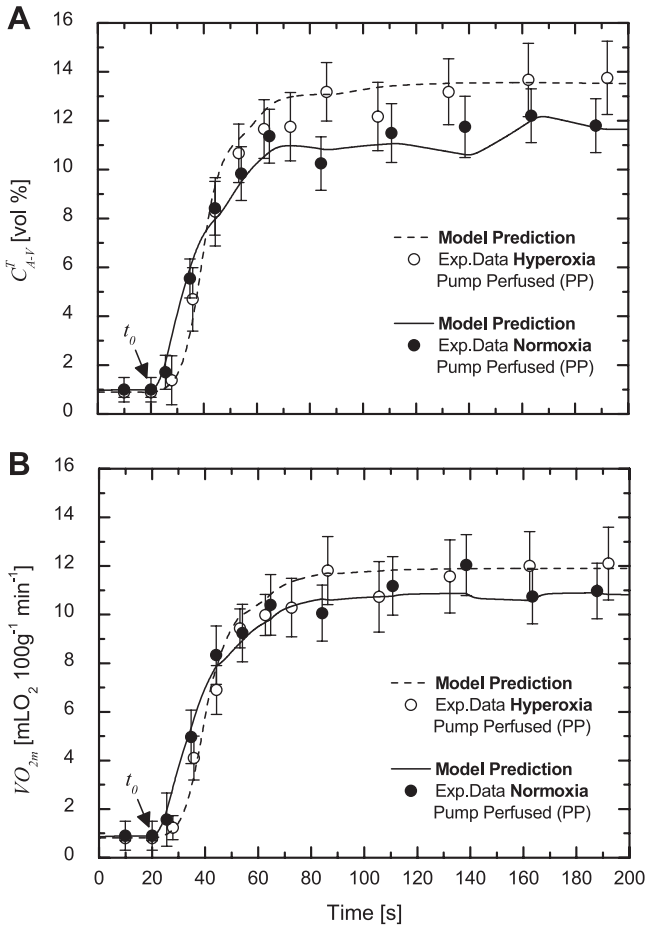

Fig. 4. Comparison between model prediction (solid and dotted lines) and experimental data on C^{T}_{A-V} (*top*) and $\dot{V}O_{2m}$ (*bottom*) responses across the gastrocnemius muscle (average value of 7 dogs, ± SE) to step change from rest to tetanic stimulus (at 60% $\dot{V}O_{2m,peak}$) obtained during hyperoxia (○) and normoxia (●) (see Refs. 22, 23) with pump perfusion (PP).

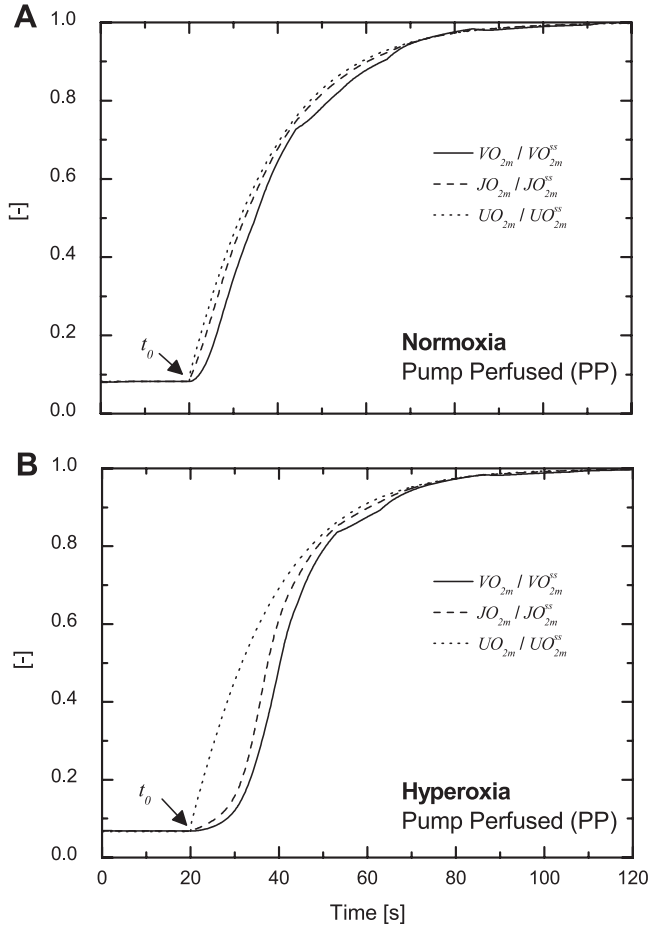

Fig. 5. Effect of oxygen content on $\dot{V}O_{2m}$, JO_{2m}, and UO_{2m} dynamic responses obtained from model simulations of gastrocnemius muscle to a step change from rest to tetanic stimulus under normoxia (*A*) and hyperoxia (*B*) with pump perfusion (PP).

Next, the simulated JO_{2m} dynamic responses to muscle contraction under normoxia were compared with those obtained with hyperoxia and hyperoxia plus RSR-13. Under both hyperoxic conditions, simulations of the average transport rate of oxygen JO_{2m} (Fig. 6*A*), oxygen partial pressures in blood $\langle PO_{2,b} \rangle$ and tissue $\langle PO_{2,c} \rangle$ (Fig. 6*B*), indicate that the diffusion gradients were almost negligible (<5 mmHg) during the first 15 s of contraction. Throughout the remaining contraction period, $\langle PO_{2,b} \rangle$ and $\langle PO_{2,c} \rangle$ decreased to different plateaus (based on free O_2 availability at contraction onset), but the

Table 4. *Simulated mean response times for muscle oxygen utilization and PCr dynamics.*

Notation	Hyperoxia + RSR-13, PP	Hyperoxia, PP	Normoxia, PP	Normoxia, SP
$\tau_{UO_{2m}}$, s	16.7	16.7	17.7	17.4
τ_{PCr}, s	16	16.2	17.9	16.3

$\tau_{UO_{2m}}$, muscle oxygen utilization; τ_{PCr}, PCr dynamics.

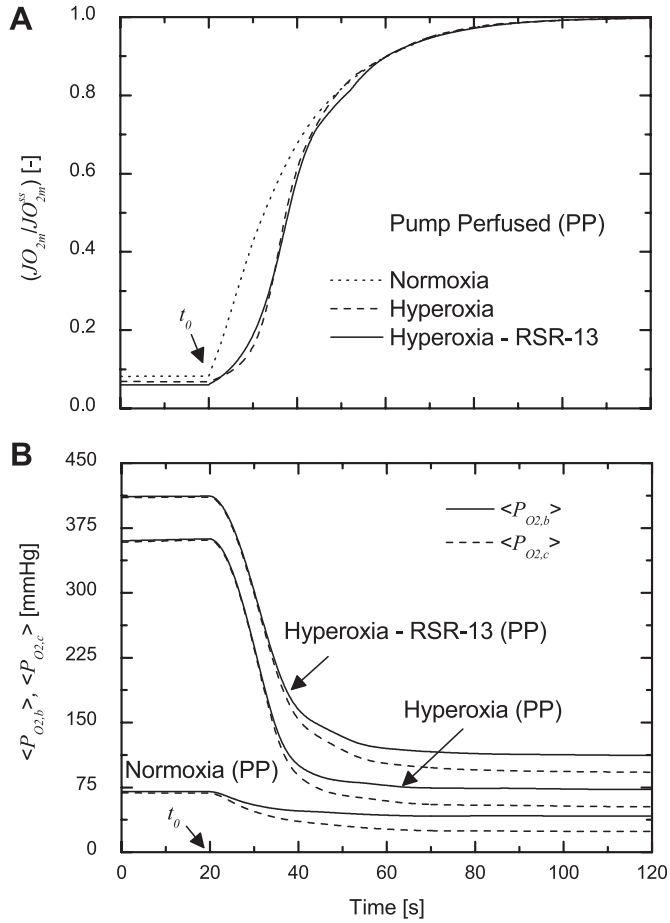

Fig. 6. Effect of oxygen content on $\dot{V}O_{2m}$, $\langle PO_{2,b}\rangle$, and $\langle PO_{2,c}\rangle$, dynamic responses. *A*: Comparison of average transport rate of oxygen between blood and muscle cells. *B*: Comparison of the dynamic responses of the average oxygen tension in blood and tissue obtained from model simulations of gastrocnemius muscle response to a step change from rest to tetanic stimulus under hyperoxia and normoxia with pump perfusion (PP).

difference between them produced a constant diffusion gradient (~20 mmHg) regardless of the oxygen content (Fig. 6*B*).

The extent of heterogeneity of oxygen was simulated in the whole muscle under various experimental conditions at rest and at 15 and 120 s of contraction onset. During hyperoxia plus RSR-13 (N1), hyperoxia (N2), and normoxia (N3), the spatial distribution of oxygen tension in blood and tissue, $PO_{2,b}$ and $PO_{2,c}$, is shown as a function of gastrocnemius muscle fraction (v/V_m) (Fig. 7). At rest, the degree of heterogeneity of oxygen in muscle was more evident during hyperoxia (Fig. 7*A*) than during normoxia (Fig. 7*B*). At the onset of the tetanic stimulus, however, $PO_{2,b}$ and $PO_{2,c}$ displayed a nonuniform distribution along the muscle volume during both hyperoxia and normoxia (Fig. 7, *A* and *B*). During hyperoxia, the heterogeneity of the distribution of $PO_{2,b}$ and $PO_{2,c}$ was more pronounced during the early stages of the transient response. This distribution became closer to that obtained during normoxia toward the steady state. At rest, at 15 and 120 s the oxygen tension distribution along the muscle was higher in hyperoxia (N1, N2) than in normoxia (N3). Moreover, the spatial distributions of $PO_{2,b}$ and $PO_{2,c}$ at given times indicated higher oxygen content during hyperoxia-RSR-13.

Prediction of metabolic fluxes and concentrations in contracting muscle. In all model simulations corresponding to the four experimental conditions investigated, metabolic fluxes and changes in metabolites concentrations were similar to those obtained at hyperoxia-RSR-13, regardless of arterial oxygen content and blood flow dynamics. Although a figure is not shown, simulated dynamic responses of $\langle \Delta\phi_{CK}\rangle$ and $\langle \phi_{OxPhos}\rangle$ fluxes are closely balanced and coordinated to maintain ATP homeostasis. Consequently, only very small changes occur in ATP concentration and the decrease in C_{PCr} mirrors the dynamics of the increase in U_{O2m}. The PCr change relative to a step change from rest to 4 min of contraction is around 45% when the stimulus corresponds to 60% of $\dot{V}O_{2m,peak}$. The dynamic responses of U_{O2m} and C_{PCr} were characterized by mean response times (Table 4; Ref. 42). As expected, the mean response times of oxygen utilization and [PCr] were similar (τ = 17 s) in all experimental conditions.

DISCUSSION

The main findings of this in silico study, which cannot be derived from experimental observations, are: *1*) the estimated dynamic response of oxygen utilization at the onset of contractions in stimulated muscle in situ is faster than that of oxygen

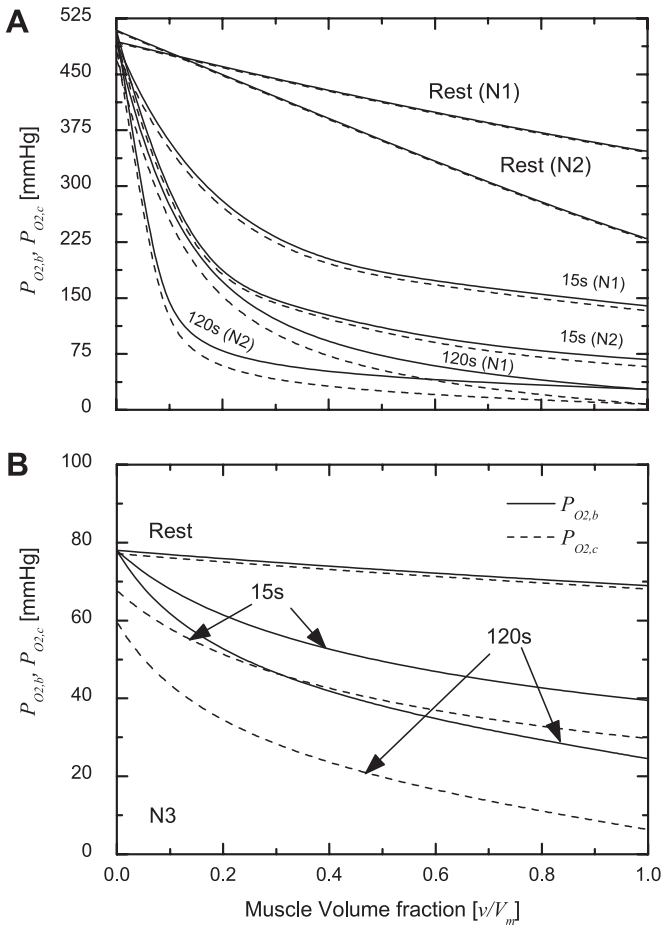

Fig. 7. Effect of oxygen content at 60% of the $\dot{V}O_{2m,peak}$ on the spatial profile of $PO_{2,b}$ and $PO_{2,c}$ as a function of the gastrocnemius muscle fraction obtained from model simulations to tetanic stimulus from rest to contraction after 15 and 120 s, under hyperoxia + RSR-13 (N1) and hyperoxia (N2) (*A*), and under normoxia (N3) with pump perfusion (PP) (*B*).

uptake; and *2*) hyperoxia does not accelerate the dynamics of the diffusion flux and consequently muscle oxygen uptake at contraction onset due to the hyperoxia-induced increase in oxygen stores.

Significance of mechanistic model. The dynamic behavior of in vivo transport and metabolic processes that occur in cells of contracting skeletal muscle is typically unavailable from experiments because it is impractical to obtain a sufficient number of frequent biopsy samples. The mathematical model developed in this study, however, can be applied to predict the dynamic behavior of such intrinsic processes as well as the transport processes between blood and cells at different levels of arterial oxygen content and blood flow. Simulations with this model quantify the effects of convection and diffusion of oxygen on the regulation of cellular respiration and bioenergetics during step transitions from rest to isometric contraction (60–70% peak muscle oxygen uptake, $\dot{V}o_{2m}$) in gastrocnemius dog muscle. Modeling the heterogeneous spatial distribution of $[O_2]$ in capillary and tissue is a major enhancement from our previous model of oxidative phosphorylation and oxygen transport in human muscles (42). This enhancement enables us to quantify more accurately the extent to which convective/diffusive processes affect the in vivo regulation of cellular respiration in an animal model of exercise (22, 23). In addition, model equations accounted for cellular ATPase, oxidative phosphorylation, and creatine kinase flux variations in skeletal muscle during exercise, where the cellular respiration is regulated by feedback control with dependence from ADP and oxygen concentrations. With this model, we are able to estimate Uo_{2m} and predict muscle metabolites dynamics in agreement with a-v $[O_2]$ differences, C^{T}_{A-V} (22, 23), as well as to make mechanistic inferences about the observed temporal profiles, instead of just characterizing their behavior by fitting empirical exponential models.

With the current model, the stimulated dynamics of $\dot{V}o_{2m}$ and C^{T}_{A-V} across the muscle were predicted and in good agreement with experimental observations under various experimental conditions. The mean response time of muscle oxygen consumption Uo_{2m} in the transition from resting steady state to muscle contraction was around 17 s (Table 4) and shorter than that of $\dot{V}o_{2m}$ (Figs. 2 and 5), regardless of the experimental condition investigated. The distinction between these dynamic responses (Uo_{2m} vs. $\dot{V}o_{2m}$) was accentuated during hyperoxia (Fig. 5*B*). An important model prediction is that higher arterial blood oxygen content ($C^{T}_{O_2,art}$) produces a longer time delay (10–15 s) in the $\dot{V}o_{2m}$ dynamic response than that obtained during normoxia (Fig. 5*A*).

Effect of hyperoxia on oxygen transport. Model simulations confirmed that the dynamic responses of muscle Uo_{2m}, $\dot{V}o_{2m}$, and Jo_{2m} at the onset of muscle contraction are distinct (Figs. 2*B* and 5). Regardless of arterial oxygen content, the dynamic response of Uo_{2m} was faster than that of $\dot{V}o_{2m}$, because oxygen uptake is determined across the muscle, while Uo_{2m} reflects intracellular oxygen utilization. In other words, $\dot{V}o_{2m}$ depends on blood flow and arteriovenous O_2 difference across the whole muscle, while Uo_{2m} is an average of the intracellular oxygen utilization that must increase at the onset of contraction to sustain a power output proportional to the imposed stimulus. Simulated Uo_{2m} dynamics at a contraction frequency of 60–70% of $\dot{V}o_{2m,peak}$ seem to be independent of the experimental conditions investigated (Table 4). In contrast, the arterial oxygen content of the blood perfusing the contracting muscle affects the dynamic responses of $\dot{V}o_{2m}$ and Jo_{2m} (Figs. 4 and 5). The higher the oxygen content of the arterial blood, the greater is the time delay between corresponding responses.

In general, Jo_{2m} depends on the diffusion gradient of oxygen and the permeability-surface area product (PS), which can increase with time in response to a stimulus (19, 20). When blood flow is constant, PS is constant also. Under this condition, simulations showed that the dynamic response of Jo_{2m} is faster than that of $\dot{V}o_{2m}$ and slower than that of Uo_{2m}. Moreover, the capillary-tissue oxygen transport rate under hyperoxia (with or without RSR-13) was smaller than that under normoxia, because the oxygen diffusion gradient, $\Delta Po_2 = \langle P_{O_2,b} \rangle - \langle P_{O_2,c} \rangle$, in hyperoxia was almost negligible during the first 10–15 s of muscle contraction (Fig. 6*A*).

While the dynamic response of Jo_{2m} is similar to that of Uo_{2m} during normoxia, the dynamic response of Jo_{2m} is similar to that of $\dot{V}o_{2m}$ during hyperoxia. These different responses depend on the availability of oxygen stores, which are larger under hyperoxia (Fig. 5*B*) than under normoxia (Fig. 5*A*). During the onset of muscle contraction (10–15 s), the larger oxygen stores under hyperoxia increase the delay time of Jo_{2m} and $\dot{V}o_{2m}$ responses. The extent of depletion of the oxygen stores was calculated as the time integral of the difference between $\dot{V}o_{2m}$ and Uo_{2m} for each experiment. For example, in normoxia the usage of oxygen stores increased from 4.7 ml/kg (when self-perfused) to 7.5 ml/kg (when pump-perfused). In hyperoxia and hyperoxia + RSR-13, the depletion of oxygen stores was even larger, reaching 13.6 and 14.1 ml/kg, respectively (47). This is consistent with experimental data in the first 10 s of muscle contraction that show $\dot{V}o_{2m}$ dynamics are not exponential (22, 23). When the oxygen stores are depleted (Fig. 6*B*), ΔPo_2 is the same for all experiments regardless of the arterial oxygen content. As a consequence, Uo_{2m}, Jo_{2m}, and $\dot{V}o_{2m}$ display similar dynamics (Fig. 6*A*) during the remainder of the contraction period (15–120 s).

Simulations of the spatially distributed model, which involve the complex interaction of oxygen convection, diffusion, and utilization, show a time delay in the dynamic response of $\dot{V}o_{2m}$. This is associated with the output $C^{T}_{O_2,ven}$ (t) that depends on the heterogeneous oxygen exchange along the muscle capillary bed (Fig. 7). The spatial profiles of $Po_{2,b}$ and $Po_{2,c}$ are higher under hyperoxia than under normoxia. This is amplified by the addition of RSR-13, which shifts the oxygen dissociation curve to the right (Fig. 7*A*). The rate of oxygen diffusion from tissue-capillaries to cells depends on the combined effect of the permeability-surface area (PS) coefficient and ΔPo_2. From both model simulation and experimental evidence under normoxic and hyperoxic conditions, oxygen stores dominate the dynamic response of capillary-tissue oxygen exchange at the onset of contraction. In contrast, PS dominates the dynamics of muscle oxygen uptake after 30 s of contraction because ΔPo_2 is almost constant (20 mmHg) even at higher oxygen content in muscle and tissue. Therefore, the oxygen gradient across the muscle is primarily determined by transport properties of the capillary and parenchymal membranes, not by the arterial oxygen content, $C^{T}_{O_2,art}$.

Mathematical model validation and limitations. With this spatially distributed model, simulations could be performed based on the anatomical volume distribution of blood and tissue and blood flow of the muscle involved during contraction. Model parameter estimated from a data subset was used to simulate responses under a variety of conditions. The simulations of the mathematical model correspond well to the dynamic data under experimental conditions with different $C^{T}_{O_2,art}$ (Figs. 2, and 4) and blood flow (Fig. 3). Thus, the model could predict C^{T}_{A-V}, as function of the stimulus time for the experiments under normoxia and hyperoxia with spontaneous and controlled blood flow. Additionally, model simulation accounts for the kinetics of oxygen stores in blood and tissue changes that are important to compute the true oxygen deficit (9, 50).

The dynamic behavior of the predicted rate of oxygen consumption is similar to that of the changes in [PCr], i.e., $\tau_{\dot{V}O_{2m}} \sim \tau_{Pcr}$, and also similar to that previously observed in humans (42). The extent of decrease in PCr from rest to contraction agrees well with data from studies of dog muscle stimulated at ~60% of $\dot{V}O_{2m,peak}$ (25). Thus, the relative change in [PCr] from its initial value (~45%) derived from model prediction is similar to that found experimentally (~40%).

In our model, $P_{O_{2,b}}$ and $P_{O_{2,c}}$ were determined by solving the basic model equation in which $\langle P_{O_{2,b}} \rangle$ and $\langle P_{O_{2,c}} \rangle$ were computed as a spatial averages along the capillary bed of the muscle. In contrast, Bohr integration assumes an arbitrary value of $\langle P_{O_{2,c}} \rangle$ (23). With Bohr integration, $\langle P_{O_{2,b}} \rangle$ values are significantly underestimated during hyperoxia compared with values computed from our more exact model (hyperoxia, 55 vs. 72.6 mmHg; hyperoxia-RSR-13, 80 vs. 112 mmHg). During normoxia, however, both methods yield $\langle P_{O_{2,b}} \rangle = 42$ mmHg.

In this model, mass transport of oxygen between capillary blood and tissue depends on the permeability-surface area coefficient (PS), which changes when the blood flow varies with time. Alternatively, PS could be considered as a function of muscle blood flow that depends on metabolic intensity (8). Although this model uses a phenomenological expression to describe the variation of PS with work rate, the simulated tissue oxygen concentration at rest is consistent with data and with the concept of capillary recruitment during exercise (19, 20, 34). Regardless of whether blood flow increases during exercise by capillary recruitment or through already recruited capillaries, the PS must change at the onset of the electrical stimulus to ensure enough oxygen supply to contracting muscle fibers to match the energy demand at any intensity. Specific experimental data are needed to quantify changes of the permeability surface area during electrical or exercise stimulus of working muscle to quantify peripheral diffusion transport and investigate capillary recruitment phenomena at the onset of contractions.

At exercise onset, model simulation (not shown) shows that net PCr breakdown ($\phi^{r}_{CK} - \phi^{f}_{CK}$) decreases C_{PCr} and that ϕ_{OxPhos} cannot produce enough ATP to maintain ATP homeostasis. These simulations are similar to those obtained in a previous study conducted in humans exercising on a cycle ergometer (42). This model of skeletal muscle metabolism provides only a limited analysis of the cellular energy balance because it does not include glycolysis as a source of ATP production. Under 60–70% of $\dot{V}O_{2m,peak}$, it has been assumed as a first approximation that the glycolytic contribution to ATP synthesis at this exercise intensity is not significant.

Additionally, previous findings (47) obtained in an analogous animal model under experimental conditions similar to those used by Grassi et al. (22, 23) support the assumption to neglect the anaerobic glycolysis contribution. However, the results of our simulation at the onset of electrical stimulus would likely be somewhat different were the glycolytic contribution taken into account.

The model equations account for cellular ATPase, oxidative phosphorylation, and creatine kinase flux variations in skeletal muscle during exercise, where cellular respiration is assumed to be regulated by feedback control with dependence from ADP and oxygen concentrations (10, 11, 12, 65, 66). However, several feedback and feedforward control models have been proposed to describe the regulation of cellular respiration in vivo. Some of the control mechanisms include: *1*) feedback control by a Michaelis-Menten relationship between oxidative phosphorylation and [ADP] (12); *2*) higher-order feedback control, using an expression in which the Hill coefficient is greater than 1 (36, 39); *3*) a more fundamental expression relating oxidative phosphorylation to the free energy of ATP hydrolysis (63); and *4*) feedback by products of ATP hydrolysis, such as inorganic phosphate (67). Other scientists have proposed feedforward mechanisms to control oxidative phosphorylation (3, 38). However, the experimental data available in the present study are not sufficient to address this issue; therefore, we adopted the approach successfully applied previously to data obtained in vivo (42).

Note also that, in our model, we assume the rate of ATP production associated with oxidative phosphorylation to be six times the rate of oxygen utilization (i.e., $\beta = 6$), but this β ratio may be as low as 3 (29, 54). An interesting analysis of the bio-energetics in working skeletal muscle proposed by di Prampero et al. (51) explains how oxygen deficit and the amount of phosphocreatine split during muscle contraction can be related to the mechanical power with measurements derived from transient and steady-state exercise responses. In particular, it has been shown that for an oxygen consumption time constant of 17 s such as in our findings, the ratio P/O_2 is close to 6. Nevertheless, when different values of β were used in the simulations, the oxidative phosphorylation dynamics remained the same at all exercise intensities, even though the values of k_{ATPase} and V_{max} differed.

The estimation of V_{max} depends on the arteriovenous oxygen dynamics, which is determined by the interplay of *1*) convection through the capillaries, *2*) diffusion between the capillary blood and tissue cells, and *3*) metabolic reactions. The blood-tissue diffusion process, which depends on the product of the permeability-surface area (PS) coefficient and the concentration gradient, may be the rate-limiting process. If PS can experimentally increased, then muscle oxygen uptake and utilization would lead to higher values of V_{max}.

Future directions. An important model extension would incorporate glycolysis because it is likely to affect the simulation at the stimulus onset (43, 61), especially at higher metabolic rates (24). A theoretical framework has been proposed to describe ATP production linking cytosolic phosphorylation state and the activity of oxidative phosphorylation and glycolysis (45), although this analysis is limited to the muscle cell.

Other extensions could include intracellular compartmentation (46) and structural and metabolic characteristics of the tissue (e.g., muscle fiber types), as well as more complex models to describe mitochondrial respiration to investigate complex physiological and pathophysiological interactions in skeletal muscle energetics (2, 5, 14). For these model extensions to be validated, more appropriate experimental data is essential.

The analysis of muscle oxygen response to exercise in human and animal models could be improved by experiments that simultaneously combine invasive and noninvasive techniques in human (16, 21, 26, 58) and animal models (6, 7, 22–24). Key measured variables include venous oxygen content, muscle blood flow, and muscle oxygenation during exercise. Measurements of muscle oxygen utilization should be as close as possible to the site of cellular respiration to assess the dynamics of oxidative phosphorylation during exercise in vivo. Measurements of ^{31}P and ^{17}O by MR spectroscopy could provide key species concentrations in oxidative phosphorylation (18, 13, 53).

The analysis of dynamic responses of the skeletal muscle depends on its volume. If the observation scale is reduced to the microvascular level, the volume of perfused tissue under consideration is uncertain. Knowing muscle volume is also essential for analyzing oxygen dynamics of the muscle microvasculature at the onset of contraction when O_2 delivery is impaired. Furthermore, the spatial distribution and temporal variation of blood flow and oxygen concentration can have a significant effect on the interpretation of the measurements (48). Without knowing the effect of muscle volume and the importance of the transient term of the oxygen balance, the quantitative evaluation of this mismatch between oxygen delivery and oxygen consumption may be interpreted incorrectly by using only the Fick principle (37, 41). Therefore, improved experimental methods are needed to obtain more precise estimates of the effective, working muscle volume during contraction.

Conclusion. A mathematical model was developed to describe the dynamic and spatial changes of O_2, ATP, and PCr concentrations in skeletal muscle from the arterial input to the venous output in response to a step increase in contractions. The temporal-spatial distributions in capillary blood and muscle cells of the extravascular tissue allow a distinct, quantitative analysis of the processes producing the arteriovenous oxygen concentration difference and muscle oxygen uptake dynamics. The dynamic response of $U_{O_{2m}}$ was faster than that of $\dot{V}_{O_{2m}}$ because the former depends on the intracellular metabolic reaction rate, whose dynamics are faster than the dynamics of transport processes in muscle. The model also predicts that the delay time between $U_{O_{2m}}$ and $\dot{V}_{O_{2m}}$ dynamic responses to contraction increases under hyperoxia, where the muscle oxygen stores are greater than normoxia.

APPENDIX

For this study, the equations describing oxygen transport in skeletal muscle are based on the model of Dash and Bassingthwaighte (15). From oxygen mass balances in capillary blood with the assumption of O_2 equilibrium between plasma and red blood cells, the dynamic spatial distribution of total oxygen concentration in capillary blood $C^T_{O_2,b}$ can be represented as:

$$\frac{\partial C^T_{O_2,b}}{\partial t} = -\frac{Q}{f_b}\frac{\partial C^T_{O_2,b}}{\partial v} + \frac{D'_b}{f_b^2}\frac{\partial^2 C^T_{O_2,b}}{\partial v^2} - \frac{PS}{f_b}(C^F_{O_2,b} - C^F_{O_2,c}) \qquad 0 \le v \le V_{mus} \tag{A1}$$

where $f_b = V_{cap}/V_{mus}$, Q is the blood volume flow, D'_b is a dispersion coefficient, and PS is the effective rate coefficient for diffusion between blood and extravascular muscle cells. The O_2 partition coefficient between blood and cells is assumed to be one. The total oxygen concentration in muscle cells $C^T_{O_2,c}$ assuming O_2 equilibrium with interstitial fluid can be represented as:

$$\frac{\partial C^T_{O_2,c}}{\partial t} = \frac{D'_c}{f_c^2}\frac{\partial^2 C^T_{O_2,c}}{\partial v^2} + \frac{PS}{f_c}(C^F_{O_2,b} - C^F_{O_2,c}) - \frac{uO_{2m}}{f_c} \qquad 0 \le v \le V_{mus} \tag{A2}$$

where $f_c = V_{tis}/V_{mus}$, uO_{2m} is the oxygen utilization rate per unit total muscle volume, and D'_c is a dispersion coefficient.

The oxygen mass balances of Eqs. 1 and 3 require a relationship between total oxygen ($C^T_{O_2,b}$, $C^T_{O_2,c}$) to free oxygen ($C^F_{O_2,b}$, $C^F_{O_2,c}$) in blood and extra-vascular muscle. To relate the total oxygen concentration C^T_x to free oxygen concentration C^F_x (x = b, c), we consider oxygen in free and (hemoglobin) bound forms in blood ($C^F_{O_2,b}$, $C^B_{O_2,b}$) and in free and (myoglobin) bound forms in muscle tissue ($C^F_{O_2,c}$, $C^B_{O_2,c}$). Consequently, the total oxygen concentrations in blood and in tissue within the muscle are the sums of the corresponding free and bound oxygen concentration:

$$C^T_{O_2,x} = C^B_{O_2,x} + C^F_{O_2,x}, \quad x \in \{b,c\} \tag{A3}$$

which are related by local chemical equilibrium. In blood the relation is

$$C^B_{O_2,b} = 4Hct\ C_{rbc,Hb}\frac{K_{Hb}(C^F_{O_2,b})^n}{1+K_{Hb}(C^F_{O_2,b})^n} \tag{A4}$$

In extravascular muscle cells, the relation is

$$C^B_{O_2,c} = W_{mc}C_{mc,Mb}\frac{K_{Mb}C^F_{O_2,c}}{1 + K_{Mb}C^F_{O_2,c}} \tag{A5}$$

These relations depend on Hb and Mb concentrations in red blood cell and myocyte ($C_{rbc,Hb}$, $C_{mc,Mb}$) and their respective volume fractions (Hct, W_{mc}). From Eq. A3, we get the differential relationships:

$$dC^T_{O_2,x} = d[C^F_{O_2,x} + C^B_{O_2,x}] = [1+dC^B_{O_2,x}/dC^F_{O_2,x}]dC^F_{O_2,x} = \gamma_x, dC^F_{O_2,x} \qquad x \in \{b,c\} \tag{A6}$$

where

$$\gamma_b = 1 + \frac{4Hct\ C_{rbc,Hb}K_{Hb}n(C^F_{O_2,b})^{n-1}}{[1 + K_{Hb}(C^F_{O_2,b})^n]^2}; \quad \gamma_C = 1 + \frac{W_{mc}\ C_{mc,Mb}K_{Mb}}{[1 + K_{Mb}C^F_{O_2,c}]^2} \tag{A7}$$

Using the relationships above, Eqs. A1 and A2 can be expressed as:

$$f_b\frac{\partial C^F_{O_2,b}}{\partial t} = -Q\frac{\partial C^F_{O_2,b}}{\partial v} + D_b\frac{\partial^2 C^F_{O_2,b}}{\partial v^2} - \frac{PS}{\gamma_b}(C^F_{O_2,b} - C^F_{O_2,c}) \qquad 0 < v < V_{mus} \qquad \forall t > 0 \tag{A8}$$

$$f_c\frac{\partial C^F_{O_2,c}}{\partial t} = D_c\frac{\partial^2 C^F_{O_2,c}}{\partial v^2} + \frac{PS}{\gamma_c}(C^F_{O_2,b} - C^F_{O_2,c}) - \frac{uO_{2m}}{\gamma_c} \qquad 0 < v < V_{mus} \qquad \forall t > 0 \tag{A9}$$

where D_b and D_c are effective dispersion coefficients.

GRANTS

This research was supported by National Institute of General Medical Sciences Grant GM-66309-01 for establishing the Center for Modeling Integrated Metabolic Systems (MIMS) at Case Western Reserve University, and by Grant NNJ06HD81G from NASA-Johnson Space Center.

REFERENCES

1. **Audi SH, Linehan JH, Krenz GS, Dawson CA.** Accounting for the heterogeneity of capillary transit times in modeling multiple indicator dilution data. *Ann Biomed Eng* 26: 914–930, 1998.
2. **Balaban R.** Modeling mitochondrial function. *Am J Physiol Cell Physiol* 291: C1107–C1113, 2006.
3. **Balaban RS.** Myocardial energy metabolism in health and disease cardiac energy metabolism homeostasis: role of cytosolic calcium. *J Mol Cell Cardiol* 34:1259–1271, 2002.
4. **Barstow TJ, Lamarra N, Whipp BJ.** Modulation of muscle and pulmonary O_2 uptakes by circulatory dynamics during exercise. *J Appl Physiol* 68: 979–989, 1990.
5. **Beard DA.** A biophysical model of the mitochondrial respiratory system and oxidative phosphorylation. *PLoS Comput Biol* 1: 252–264, 2005.
6. **Behnke BJ, Kindig CA, McDonough P, Poole DC, Sexton WL.** Dynamics of microvascular oxygen pressure during rest-contraction transition in skeletal muscle of diabetic rats. *Am J Physiol Heart Circ Physiol* 283: H926–H932, 2002.
7. **Behnke BJ, Padilla DJ, Ferreira LF, Delp MD, Musch TI, Poole DC.** Effects of arterial hypotension on microvascular oxygen exchange in contracting skeletal muscle. *J Appl Physiol* 100: 1019–1026, 2006.
8. **Caldwell JH, Martin GV, Raymond GM, Bassingthwaighte JB.** Regional myocardial flow and capillary permeability-surface area products are nearly proportional. *Am J Physiol Heart Circ Physiol* 267: H654–H666, 1994.
9. **Cerretelli P, di Prampero PE.** Gas exchange in exercise. In: *Handbook of Physiology*. *The Respiratory System*. *Gas Exchange*. Bethesda, MD: Am Physiol Soc, 1987, sect. 3, vol. IV, chapt. 16, p. 297–340.
10. **Chance B, Williams GR.** Respiratory enzymes in oxidative phosphorylation. I. Kinetics of oxygen utilization. *J Biol Chem* 217: 383–393, 1955.
11. **Chance B, Williams GR, Holmes WF, Higgins J.** Respiratory enzymes in oxidative phosphorylation. V. A mechanism for oxidative phosphorylation. *J Biol Chem* 217: 439–451, 1955.
12. **Chance B, Leigh JS Jr, Kent J, McCully K, Nioka S, Clarkii BJ, Maris JM, Graham T.** Multiple controls of oxidative metabolism in living tissues as studied by phosphorus magnetic resonance. *Proc Natl Acad Sci USA* 83: 9458–9462, 1986.
13. **Chung Y, Mole PA, Sailasuta N, Tran TK, Hurd R, Jue T.** Control of respiration and bioenergetics during muscle contraction. *Am J Physiol Cell Physiol* 288: C730–C738, 2005.
14. **Cortassa S, Aon MA, O'Rourke B, Jacques R, Tseng HJ, Marbăn E, Winslow RL.** A computational model integrating electrophysiology, contraction, and mitochondrial bioenergetics in the ventricular myocyte. *Biophys J* 91: 1564–1589, 2006.
15. **Dash RK, Bassingthwaighte JB.** Simultaneous blood-tissue exchange of oxygen, carbon dioxide, bicarbonate, and hydrogen ion. *Ann Biomed Eng* 34: 1129–1148, 2006.
16. **DeLorey DS, Kowalchuk JM, Paterson DH.** Relationship between pulmonary O_2 uptake kinetics and muscle deoxygenation during moderate-intensity exercise. *J Appl Physiol* 95: 113–120, 2003.
17. **Dennis JE, Gay DM, Welsch RE.** Algorithm 573: NL2SOL—an adaptive nonlinear least-squares algorithm. *ACM Trans Math Softw* 7: 348–383, 1981.
18. **Fiat D, Dolinsek J, Hankiewicz J, Dujovny M, Ausman J.** Determination of regional cerebral oxygen consumption in the human: ^{17}O natural abundance cerebral magnetic resonance imaging and spectroscopy in a whole body system. *Neurol Res* 15: 237–48, 1993.
19. **Frisbee JC, Barclay JK.** Microvascular hematocrit and permeability-surface area product in contracting canine skeletal muscle in situ. *Microvasc Res* 55: 153–164, 1998.
20. **Frisbee JC, Barclay JK.** Microvascular hematocrit and permeability-surface area product of in situ canine skeletal muscle during fatigue. *Microvasc Res* 57: 203–207, 1999.
21. **Grassi B, Poole DC, Richardson RS, Knight DR, Erickson BK, Wagner PD.** Muscle O_2 uptake kinetics in humans: implications for metabolic control. *J Appl Physiol* 80: 988–998, 1996.
22. **Grassi B, Gladden LB, Samaja M, Stary CM, Hogan MC.** Faster adjustment of O_2 delivery does not affect $\dot{V}O_2$ on-kinetics in isolated in situ canine muscle. *J Appl Physiol* 85: 1394–1403, 1998.
23. **Grassi B, Gladden LB, Stary CM, Wagner PD, Hogan MC.** Peripheral O_2 diffusion does not affect $\dot{V}O_2$ on-kinetics in isolated in situ canine muscle. *J Appl Physiol* 85: 1404–1412, 1998.
24. **Grassi B, Hogan MC, Kelley KM, Aschenbach WG, Hamann JJ, Evans RK, Patillo RE, Gladden LB.** Role of convective O_2 delivery in determining $\dot{V}O_2$ on-kinetics in canine muscle contracting at peak $\dot{V}O_2$. *J Appl Physiol* 89: 1293–1301, 2000.
25. **Grassi B, Hogan MC, Greenhaff PL, Hamann JJ, Kelley KM, Aschenbach WG, Constantin D, Gladden LB.** Oxygen uptake on-kinetics in dog gastrocnemius in situ following activation of pyruvate dehydrogenase by dichloroacetate. *J Physiol* 538: 195–207, 2002.
26. **Grassi B, Pogliaghi S, Rampichini S, Quaresima V, Ferrari M.** Muscle oxygenation and pulmonary gas exchange kinetics during cycling exercise on-transitions in humans. *J Appl Physiol* 95: 149–158, 2003.
27. **Grassi B.** Delayed metabolic activation of oxidative phosphorylation in skeletal muscle at exercise onset. *Med Sci Sports Exerc* 37: 1567–1573, 2005.
28. **Hindmarsh AC.** ODEPACK—a systematized collection of ODE solvers. In:*Scientific Computing*, edited by Stepleman RS. Amsterdam: North-Holland, 1983, p. 55–64.
29. **Hinkle PC.** P/O ratios of mitochondrial oxidative phosphorylation. *Biochim Biophys Acta* 1706: 1–11, 2005.
30. **Hochachka PW.** Solving the common problem: matching ATP synthesis to ATP demand during exercise. *Adv Vet Sci Comp Med* 38A: 41–56, 1994.
31. **Hochachka PW, McClelland GB.** Cellular metabolic homeostasis during large-scale change in ATP turnover rates in muscles. *J Exp Biol* 200: 381–386, 1997.
32. **Hogan MC, Arthur PG, Bebout DE, Hochachka PW, Wagner PD.** O_2 in regulating tissue respiration in dog muscle working in situ. *J Appl Physiol* 73: 728–736, 1992.
33. **Hogan MC, Willford DC, Keipert PE, Faithfull NS, Wagner PD.** Increased plasma O_2 solubility improves O_2 uptake of in situ dog muscle working maximally. *J Appl Physiol* 73: 2470–2475, 1992.
34. **Honig CR, Odoroff CL, Frierson JL.** Capillary recruitment in exercise: rate, extent, uniformity, and relation to blood flow. *Am J Physiol Heart Circ Physiol* 238: H31–H42, 1980.
35. **Hughson RL, Kowalchuk JM.** Kinetics of oxygen uptake for submaximal exercise in hyperoxia, normoxia, and hypoxia. *Can J Appl Physiol* 20: 198–210, 1995.
36. **Jeneson JA, Westerhoff HV, Brown TR, Van Echteld CJ, Berger R.** Quasi-linear relationship between Gibbs free energy of ATP hydrolysis and power output in human forearm muscle. *Am J Physiol Cell Physiol* 268: C1474–C1484, 1995.
37. **Kemp G.** Kinetics of muscle oxygen use, oxygen content, and blood flow during exercise. *J Appl Physiol* 99: 2463–2468, 2005.
38. **Korzeniewski B.** Regulation of ATP supply in mammalian skeletal muscle during resting state intensive work transition. *Biophys Chem* 83: 19–34, 2000.
39. **Kushmerick MJ.** Energy balance in muscle activity: simulations of ATPase coupled to oxidative phosphorylation and to creatine kinase. *Comp Biochem Physiol B Biochem Mol Biol* 120: 109–123, 1998.
40. **Lai N, Dash RK, Nasca MM, Saidel GM, Cabrera ME.** Relating pulmonary oxygen uptake to muscle oxygen consumption at exercise onset: in vivo and in silico studies. *Eur J Appl Physiol* 97: 380–394, 2006.
41. **Lai N, Syed N, Saidel GM, Cabrera ME.** Muscle oxygen uptake differs from consumption dynamics during transients in exercise. *Advances in Experimental Medicine and Biology*: ISOTT XXIX, 2006.
42. **Lai N, Camesasca M, Saidel GM, Dash RK, Cabrera ME.** Linking pulmonary oxygen uptake, muscle oxygen utilization and cellular metabolism during exercise. *Ann Biomed Eng* 35: 956–968, 2007.
43. **Lambeth MJ, Kushmerick MJ.** A computational model for glycogenolysis in skeletal muscle. *Ann Biomed Eng* 30: 808–827, 2002.
44. **Millikan GA.** Muscle hemoglobin. *Physiol Rev* 19: 503–523, 1939.
45. **Mader A.** Glycolysis and oxidative phosphorylation as a function of cytosolic phosphorylation state and power output of the muscle cell. *Eur J Appl Physiol* 88: 317–338, 2003.
46. **Ovadi J, Saks V.** On the origin of intracellular compartmentation and organized metabolic systems. *Mol Cell Biochem* 256–257: 5–12, 2004.

47. **Piiper J, Di Prampero PE, Cerretelli P.** Oxygen debt and high-energy phosphates in gastrocnemius muscle of the dog. *Am J Physiol* 215: 523–531, 1968.
48. **Pittman RN.** Oxygen supply to contracting skeletal muscle at the microcirculatory level: diffusion vs. convection. *Acta Physiol Scand* 168: 593–602, 2000.
49. **Poole DC, Behnke BJ, Padilla DJ.** Dynamics of muscle microcirculatory oxygen exchange. *Med Sci Sports Exerc* 37: 1559–1566, 2005.
50. **di Prampero PE, Boutellier U, Pietsch P.** Oxygen deficit and stores at onset of muscular exercise in humans. *J Appl Physiol* 55: 146–153, 1983.
51. **di Prampero PE, Francescato MP, Cettolo V.** Energetics of muscular exercise at work onset: the steady-state approach. *Pflügers Arch* 445: 741–746, 2003.
52. **Richardson RS, Tagore K, Haseler LG, Jordan M, Wagner PD.** Increased $\dot{V}_{O_2\,max}$ with right-shifted Hb-O_2 dissociation curve at a constant O_2 delivery in dog muscle in situ. *J Appl Physiol* 84: 995–1002, 1998.
53. **Rossiter HB, Ward SA, Howe FA, Kowalchuk JM, Griffiths JR, Whipp BJ.** Dynamics of intramuscular ^{31}P-MRS P_i peak splitting and the slow components of PCr and O_2 uptake during exercise. *J Appl Physiol* 93: 2059–2069, 2002.
54. **Salway JG.** *Metabolism at a Glance* (3rd ed.). Oxford: Blackwell Publishing, 2004.
55. **Schiesser WE, Silebi CA.** *Computational Transport Phenomena: Numerical Methods for the Solution of Transport Problems.* Cambridge: Cambridge University, 1997.
56. **Smith SG.** Normal hemoglobin formation in the dog. *Am J Physiol* 182: 433–438, 1955.
57. **Territo PR, French SA, Dunleavy MC, Evans FJ, Balaban RS.** Calcium activation of heart mitochondrial oxidative phosphorylation. *J Biol Chem* 276: 2586–2599, 2001.
58. **Tordi N, Mourot L, Matusheski B, Hughson RL.** Measurements of cardiac output during constant exercises: comparison of two non-invasive techniques. *Int J Sports Med* 25: 145–149, 2004.
59. **Tschakovsky ME, Hughson RL.** Interaction of factors determining oxygen uptake at the onset of exercise. *J Appl Physiol* 86: 1101–1113, 1999.
60. **Vicini P, Kushmerick MJ.** Cellular energetics analysis by a mathematical model of energy balance: estimation of parameters in human skeletal muscle. *Am J Physiol Cell Physiol* 279: C213–C224, 2000.
61. **Vinnakota K, Kemp ML, Kushmerick MJ.** Dynamics of muscle glycogenolysis modeled with pH time course computation and pH-dependent reaction equilibria and enzyme kinetics. *Biophys J* 91: 1264–1287, 2006.
62. **Walsh B, Howlett RA, Stary CM, Kindig CA, Hogan MC.** Determinants of oxidative phosphorylation onset kinetics in isolated myocytes. *Med Sci Sports Exerc* 37: 1551–1558, 2005.
63. **Westerhoff HV, Van Echteld CJ, Jeneson JA.** On the expected relationship between Gibbs energy of ATP hydrolysis and muscle performance. *Biophys Chem* 54: 137–142, 1995.
64. **Whipp BJ, Rossiter HB, Ward SA, Avery D, Doyle VL, Howe FA, Griffiths JR.** Simultaneous determination of muscle ^{31}P and O_2 uptake kinetics during whole body NMR spectroscopy. *J Appl Physiol* 86: 742–747, 1999.
65. **Wilson DF, Owen CS, Holian A.** Control of mitochondrial respiration: a quantitative evaluation of the roles of cytochrome C and oxygen. *Arch Biochem Biophys* 182: 749–762, 1977.
66. **Wilson DF, Erecinska M, Drown C, Silver IA.** The oxygen dependence of cellular energy metabolism. *Arch Biochem Biophys* 195: 485–493, 1979.
67. **Wu F, Jeneson JA, Beard DA.** Oxidative ATP synthesis in skeletal muscle is controlled by substrate feedback. *Am J Physiol Cell Physiol* 292: C115–C124, 2007.
68. **Zhou H, Saidel GM, Cabrera ME.** Multi-organ system model of O_2 and CO_2 transport during isocapnic and poikilocapnic hypoxia. *Respir Physiol Neurobiol* 156: 320–330, 2007.